

Published in final edited form as:

Angew Chem Int Ed Engl. 2013 December 23; 52(52): 13958–13964. doi:10.1002/anie.201308986.

Biodegradable Gold Nanovesicles with Ultra-Strong Plasmonic Coupling Effect for Photoacoustic Imaging and Photothermal Therapy**

Peng Huang[#],

Laboratory of Molecular Imaging and Nanomedicine (LOMIN), National Institute of Biomedical Imaging and Bioengineering (NIBIB), National Institutes of Health (USA)

Jing Lin[#],

Department of Chemistry and Biochemistry, University of Maryland, College Park, Maryland 20742 (USA)

Wanwan Li,

Laboratory of Molecular Imaging and Nanomedicine (LOMIN), National Institute of Biomedical Imaging and Bioengineering (NIBIB), National Institutes of Health (USA)

Pengfei Rong,

Laboratory of Molecular Imaging and Nanomedicine (LOMIN), National Institute of Biomedical Imaging and Bioengineering (NIBIB), National Institutes of Health (USA)

Zhe Wang,

Laboratory of Molecular Imaging and Nanomedicine (LOMIN), National Institute of Biomedical Imaging and Bioengineering (NIBIB), National Institutes of Health (USA)

Center for Molecular Imaging and Translational Medicine, School of Public Health, Xiamen University, Xiamen 361005, China

Shouju Wang,

Laboratory of Molecular Imaging and Nanomedicine (LOMIN), National Institute of Biomedical Imaging and Bioengineering (NIBIB), National Institutes of Health (USA)

Xiaoping Wang,

Laboratory of Molecular Imaging and Nanomedicine (LOMIN), National Institute of Biomedical Imaging and Bioengineering (NIBIB), National Institutes of Health (USA)

Xiaolian Sun,

Laboratory of Molecular Imaging and Nanomedicine (LOMIN), National Institute of Biomedical Imaging and Bioengineering (NIBIB), National Institutes of Health (USA)

Maria Aronova,

**This work was supported, by the startup funds from the University of Maryland, the Intramural Research Program (IRP) of the NIBIB, NIH, the National Key Basic Research Program (973 Project) (2010CB933901, 2013CB733802, 2014CB744503), the National Science Foundation of China (81272987, 31170961, 51102258, 81371596), and the Chinese Academy of Sciences professorship for Senior International Scientists (2011T2J06).

[#]shawn.chen@nih.gov; shawn@umd.edu.

Supporting information for this article is available on the WWW under <http://www.angewandte.org> or from the author.

Laboratory of Cellular Imaging and Macromolecular Biophysics, NIBIB, National Institutes of Health (USA)

Gang Niu,

Laboratory of Molecular Imaging and Nanomedicine (LOMIN), National Institute of Biomedical Imaging and Bioengineering (NIBIB), National Institutes of Health (USA)

Richard D. Leapman,

Laboratory of Cellular Imaging and Macromolecular Biophysics, NIBIB, National Institutes of Health (USA)

Zhihong Nie^{*}, and

Department of Chemistry and Biochemistry, University of Maryland, College Park, Maryland 20742 (USA)

Xiaoyuan Chen^{*}

Laboratory of Molecular Imaging and Nanomedicine (LOMIN), National Institute of Biomedical Imaging and Bioengineering (NIBIB), National Institutes of Health (USA)

[#] These authors contributed equally to this work.

Abstract

Hierarchical assembling of gold nanoparticles (GNPs) allows one to engineer the localized surface plasmon resonance (LSPR) peaks to the near-infrared (NIR) region for enhanced photothermal Therapy (PTT). Herein we report a novel theranostic platform based on biodegradable plasmonic gold nanovesicles for photoacoustic (PA) Imaging and PTT. The disulfide bond (S-S) termed PEG-*b*-PCL block copolymer graft allows dense packing of GNPs during the assembly process and induces ultra-strong plasmonic coupling effect between adjacent GNPs. The strong NIR absorption induced by plasmon coupling and very high photothermal conversion efficiency ($\eta = 37\%$) enable simultaneous thermal/PA imaging and enhanced PTT efficacy with improved clearance of the dissociated particles after the completion of PTT. These vesicle-architectures assembling of various nanocrystals with tailored optical, magnetic, and electronic properties opens new possibilities for constructing multifunctional biodegradable platforms for biomedical applications, particularly in cancer theranotics.

Keywords

Theranostics; Biodegradable block co-polymer; Gold Nanovesicles; Plasmonic Coupling Effect; Photoacoustic Imaging; Photothermal Therapy

Photothermal therapy (PTT), due to its specific spatial/temporal selectivity and minimal invasiveness, has been increasingly recognized in cancer treatment.^[1] Various inorganic/organic nanomaterials have been used as photothermal conversion agents (PTCAs).^[2] However, most of these agents have not yet achieved clinical application, most likely due to their poor pharmacokinetics and potential long-term toxicity.^[3] An ideal PTCA is expected to have the following features: i) Strong absorbance in the near-infrared (NIR) region, which has minimal absorbance for skin, tissues, and hemoglobin.^[2f, 3] ii) High photothermal conversion efficiency and good thermal conductivity, *via* fast absorption of optical energy,

instant conversion into heat, and rapid transmission to the surrounding tissues/cells. iii) Good biocompatibility and biodegradability,^[2b, 3] with little to no toxicity and easy clearance from the body. iv) Convenient and real-time visualization of *in vivo* PTCA delivery, distribution and monitoring of treatment efficacy.^[4]

Plasmonic PTCAs, particularly gold-based nanostructures that can absorb and transfer optical energy into heat by the Landau damping effect with high efficiency, have received great interest in PTT.^[5] Early clinical studies with Auroshell (polyethylene glycol 500 coated gold nanoshells (GNSs) sized in 150 nm) have shown some promise in cancer PTT treatment but the large nanoparticles tend to have slow excretion from the body.^[6] For gold nanorods (GNRs), the toxicity derived from the cetyltrimethylammonium bromide (CTAB) surfactant during the synthesis severely limits their biomedical applications.^[1b, 5c] For gold nanoparticles (GNPs), their absorptions are not optimal for PTT,^[5b, 7] with the localized surface plasmon resonance (LSPR) peaks at 520 nm for 10 nm GNPs and 580 nm for 100 nm GNPs. Hierarchical assembling of GNPs allows one to engineer the LSPR peaks to the NIR region for enhanced PTT with improved clearance after the dissociation of assemblies. Recently, we have demonstrated that vesicular/clustered GV assemblies composed of poly(ethyl oxide)-*b*-polystyrene (PEG-*b*-PS) tethered GNPs have LSPR absorbance in the range of 650~800 nm due to plasmon coupling between adjacent GNPs.^[8] However, the PEG-*b*-PS polymer based assemblies are nonbiodegradable and bear suboptimal photothermal conversion efficiency. It is thus highly desirable to further develop novel biodegradable polymer/GNPs assemblies with high photothermal conversion efficiency for PTT, leading to the breakdown of vesicles into smaller discrete GNPs after the completion of PTT, followed by rapid clearance of the dissociated particles.

Here we report a novel design of biodegradable gold nanovesicles (BGVs) composed of poly(ethylene glycol)-*b*-poly(ϵ -caprolactone) (PEG-*b*-PCL) tethered GNPs with ultra-strong plasmonic coupling effect for photoacoustic (PA) imaging and PTT (**Scheme 1** and **S1**). The disulfide bond (S-S) termed PEG-*b*-PCL polymer was grafted onto the surface of GNPs, and then guided the formation of BGVs in THF/water system by a dialysis method. This PEG-*b*-PCL polymer graft can reduce the distance (*d*) between adjacent GNPs during the assembly process, which induces ultra-strong plasmonic coupling effect. The formation of abundant inter-nanoparticle junctions can tune the LSPR peak of the original GNPs from visible to NIR region. The BGVs with strong absorbance in the NIR region show excellent PA response and enhanced photothermal conversion efficiency upon laser irradiation.

GNPs with a diameter of 26.2 ± 1.45 nm were prepared by using citrate to reduce chloroauric acid in aqueous phase. Plasmonic BGVs were prepared by assembling GNPs tethered with S-S-termed amphiphilic block copolymer (BCP), PEO₄₅-*b*-PCL₂₇₀ ($M_n = 24.4$ Kg/mol, PDI = 1.22), followed by the dialysis of a tetrahydrofuran (THF) solution of concentrated GNPs in water. The self-assembly of PEG-*b*-PS tethered GNPs into GVs was prepared according to our previous report.^[9] The self-assembly process is governed by the balance of attractive forces, namely hydrophilic/hydrophobic interactions of amphiphilic BCPs. The representative SEM and TEM images in **Figure 1a-c** showed the well-defined vesicular assemblies of GNPs. The BGVs are composed of a single layer of seamlessly packed GNPs in the vesicular membranes. The hollow interior of the assemblies was clearly

confirmed by the morphology of broken BGVs (The inset of Figure 1a). As shown in **Figure 1c**, due to the presence of rigid benzene rings in the polystyrene part of PEG-*b*-PS, the GNPs are more separated from each other in the GVs, than in the BGVs with more flexible PEG-*b*-PCL tether.

To better understand how the BGVs are formed, we varied the concentrations of the THF solution of GNPs (12.5, 37.5, 50, 100, 150 and 250 µg/mL) during the dialysis in water. As shown in **Figure S3**, the BGVs were produced when the GNP concentration is more than 50 µg/mL. At lower GNP concentrations (<50 µg/mL), gold clusters are formed instead. When the GNP concentration was over 100 µg/mL, almost all the GNPs were assembled into BGVs. The size of BGVs is dependent on the concentration of GNPs (**Figure S4**). At GNP concentration of 100 and 150 µg/mL, the BGVs exhibited a relatively narrow size distribution of 192.6 ± 11.8 and 207.3 ± 15.7 nm, respectively. When the GNP concentration reached 250 µg/mL, huge sub-micron sized BGVs were formed. Assembly of GNPs leads to short interparticle distance, thus a red-shift in extinction spectra due to strong plasmonic coupling effect between adjacent GNPs.^[10] This process is accompanied with a color change of the solution from red to dark blue (**Figure S5**). For the GVs composed of PEG-*b*-PS tethered GNPs, the LSPR peak shifted from 518 to 630 nm (**Figure 1d and S5**). For the BGVs composed of PEG-*b*-PCL tethered GNPs, the LSPR peaks are broadened and the major peak moves to 808 (BGV1), 902 (BGV2) and 1008 (BGV3) nm by increasing the GNP concentration.

The strong NIR absorbance of BGV1 around 800 nm motivated us to investigate their potential in PTT of cancer with an 808 nm laser. Different gold nanomaterials were dispersed in water, and then irradiated with suitable laser (**Figure 2a**). No obvious temperature change was observed in the control group of pure water. Upon laser illumination for 5 min (laser power: 1 W/cm²), GNPs, GNRs, GVs, and BGVs raised the temperature by 8.0, 24.0, 23.6, and 40.7 °C, respectively. The photothermal effect of BGVs could increase monotonically with particle concentration and radiant energy (**Figure S6**).

Next, we measured the photothermal conversion efficiency (η) of BGVs. The η value was calculated according to the energy balance on the system as follows^[2c, 2h, 4c, 11]:

$$\eta = (hS \Delta T_{max} - Q_s) / I (1 - 10^{-A_{808}}) \quad (1)$$

$$\tau_s = m_D C_D / hS \quad (2)$$

where h is the heat transfer coefficient, S is the surface area of the container, ΔT_{max} is the temperature change of the BGV solution at the maximum steady-state temperature, I is the laser power, A_{808} is the absorbance of BGVs at 808 nm, and Q_s is the heat associated with the light absorbance of the solvent. τ_s is the sample system time constant, m_D and C_D are the mass (0.2 g) and heat capacity (4.2 J/g) of deionized water used as the solvent.

According to Equations 1 and 2, the η value of BGVs was determined to be 37% (**Figure S7**). The η value of BGVs is markedly higher than GVs (18%), GNRs (22%) and GNSs

(13%)^[11] (**Figure 2b**), suggesting high efficiency of BGVs to convert the 808 nm laser energy into heat due to the presence of ultra-strong plasmonic coupling effect.

We further investigated the biodegradability of BGVs by treating them at different conditions. We found that the assembled BGVs gradually collapsed by increasing the temperature of BGVs solution (**Figure 2c**). When the system temperature was over 70 °C, majority of BGVs were dissociated after 10 min since the melting point of PCL is about 60°C.^[12] As shown in **Figure S8**, we found that small holes appeared on the membranes of BGVs at 1-week time. Afterwards, defects between adjacent GNPs became more evident and major fragments falling off the vesicles were seen in 4 weeks. Finally, all of BGVs are completely collapsed at 8 week. Based on those results, we predict the *in vivo* dissociation of BGVs will be shorter, due to the complex body conditions including abundant enzymes. These results suggest that the BGVs can be gradually degraded into discrete GNPs by both temperature-dependent and time-dependent manners.

NIR laser-triggered cell killing effect of BGVs was assessed by a standard (3-[4,5-dimethylthiazol-2-yl]-2,5 diphenyl tetrazolium bromide) (MTT) assay^[13] (**Figure S9a**). Cell viability was normalized to the control group without any treatment. Without laser irradiation, BGVs exhibited negligible toxicity to MDA-MB-435 cells. Upon laser irradiation, BGVs induced a concentration and laser dose-dependent cytotoxicity to MDA-MB-435 cells. The cell viability of irradiated groups gradually decreased with the increase of BGV concentration. With the extension of the treatment to 10 min, almost all cells were killed at all tested concentrations. To further identify the cell viability, the cells were co-stained by Calcein AM and ethidium homodimer-1 to differentiate live (green) and dead (red) cells (**Figure S9b-d**), respectively. In the control group, all the cells displayed green fluorescence, which suggests that laser irradiation alone is not able to kill tumor cells. In the BGV group, all cells were killed, as indicated by the intense homogeneous red fluorescence. Meanwhile, we found that all cells within laser spot were killed, while cells without irradiation (outside the region of laser spot) displayed green fluorescence. This result indicates that PTT treatment using BGVs is highly selective and localized.

Encouraged by the *in vitro* PTT effect of BGVs, we then investigated the feasibility of using BGVs for *in vivo* PT/PA imaging and PTT in a MDA-MB-435 tumor xenograft model. When the tumors reached about 60 mm³, the mice were treated with intratumoral injection of 50 µL of BGVs (400 µg/mL). Thermal imaging was employed to monitor the efficacy of treatment *in vivo* using an infrared thermal camera (**Figure 3a-b**). Under both 0.5 and 1 W/cm² 808 nm laser irradiation, the local tumor temperature was rapidly increased over 18 °C within 5 min, which was high enough to kill tumor cells *in vivo*. No significant temperature rising was observed in other body parts of the mice (**Figure S10**). With intratumoral administration of the same amount of GNRs followed by 1 W/cm² 808 nm laser irradiation, the local temperature change was about 10 °C within 5 min. With intratumoral administration of the same amount of GVs and 2 W/cm² 671 nm laser irradiation, the local temperature change was about 8 °C within 5 min.

PA imaging was employed to evaluate the PA property of BGVs, and guide the intratumoral injection (**Video S1**). With the increase of BGV concentration, the PA signal intensity was

linearly correlated with the BGV concentration ($R^2 = 0.994$), described by the following typical equation: $Y = 0.16 + 46.50X$. (**Figure 3c**). Compared with GNRs (**Figure S11**), BGVs showed much stronger PA signal at the same OD @808 nm value. Intense PA signals were observed in the tumor region injected with BGVs (**Figure 3d and Figure S12**). As shown in **Figure 3e**, the average tumor PA intensity of BGVs was ~10-fold stronger than that before BGV injection, and ~1-fold stronger than that of GV injection.

Finally, the BGVs-induced PTT effect *in vivo* was studied. Considering the size of BGVs over 200 nm, they are efficient in activating the human complement system and are hence cleared rapidly from the blood circulation and predominantly taken up by the reticuloendothelial system (RES) including the liver (Kupffer cells) and the spleen (marginal zone and red pulp) macrophages.^[14] Therefore, the preferred route of BGV administration is intratumoral injection, which is the most efficient way for delivery of PTCA in PTT.^[15] As shown in **Figure 4a**, seven groups of MDA-MB-435 tumor-bearing mice with 5–7 mice per group were used in our experiment. For the treatment groups ($n = 7/\text{group}$), mice were intratumorally injected with 50 μL of BGVs (400 $\mu\text{g/mL}$) and then irradiated by the 808 nm laser at power densities of 0.5 or 1 W/cm^2 for 5 min. Other control groups of mice (5 mice/group) included untreated mice, mice with BGV administration but no laser, mice with laser irradiation only, mice with GNR administration and 808 nm laser irradiation (0.5 W/cm^2), and mice with GV administration and 671 nm laser irradiation (2 W/cm^2). GNR, GV and BGV administration/irradiation groups showed remarkable delay in tumor growth or tumor regression compared with the control groups after two weeks (GNR vs. Ctl, $P < 0.001$; GV vs. Ctl, $P < 0.001$; BGV vs. Ctl, $P < 0.0001$). In the BGVs + laser groups (both 0.5 and 1 W/cm^2), all the tumors were effectively ablated, leaving black scars at their original sites without showing reoccurrence (**Figure 4a and b**). In contrast, the tumors in the control groups showed similar growth speed (**Figure 4a**). It is worth noting that the BGV group with low dose of laser irradiation (0.5 W/cm^2 for 5 min) exhibited significantly higher therapeutic efficacy as compared with GNR/laser and GV/laser groups on day 14 (BGV vs. GV, $P < 0.0001$; BGV vs. GNR, $P < 0.0001$). While mice in the control groups showed average life spans of 14~20 days since treatment started, mice in the BGV treated groups were tumor-free and survived over 30 days without a single death or tumor reoccurrence, mice in the GNR/laser group showed only slight delay of tumor growth and all the animals at day 24 had to be sacrificed due to the extensive tumor burden (**Figure 4c**). Hematoxylin and eosin (H&E) staining of tumor slices was also carried out for tumors collected immediately after laser irradiation (**Figure 4e**). We found significant cancer cell damage in the tumor of the BGV/laser group, but not in the other three control groups. We also investigated the biodistribution of BGVs after intratumoral injection. **Figure 4d** showed that BGVs would leak into circulation and prominently accumulate in the RES including the liver and spleen on day 2. BGVs were cleared from the RES on day 8. For BGVs only group, the BGVs always stay in the tumor tissues (Data not shown). These results indicate that BGVs have excellent theranostic capability for PT/PA imaging and PTT of tumor with reasonable clearance most likely due to the dissociation of assemblies after laser irradiation and under the physiological condition over time.

In summary, we have developed a novel theranostic platform based on biodegradable plasmonic gold vesicles for cancer imaging and treatment. The disulfide bond-termed PEG-*b*-PCL BCP graft allows dense packing of GNPs with specific interparticle orientations during the assembly process and induces ultra-strong plasmonic coupling effect between adjacent GNPs. The strong NIR absorption induced by plasmon coupling enables thermal/PA imaging and PTT with high efficacy. The BGVs we developed have the following features: i) high photothermal conversion efficiency ($\eta = 37\%$); ii) dissociation into discrete gold nanoparticles at elevated temperatures; iii) simultaneous thermal/PA imaging and enhanced PTT efficacy; iv) improved clearance of the dissociated particles after the completion of PTT. In addition, the multifunctional BGVs have high solubility and stability in aqueous media, good biocompatibility, thus facilitating their biomedical applications.

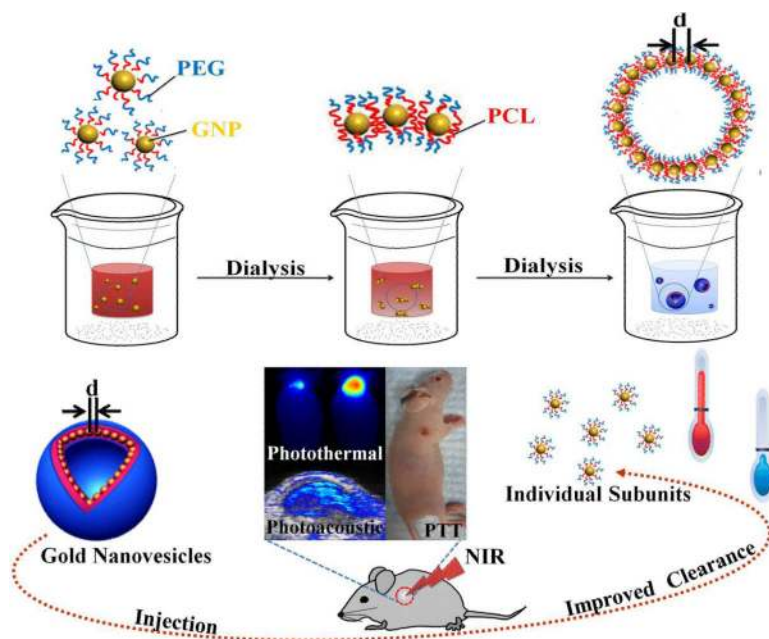
Supplementary Material

Refer to Web version on PubMed Central for supplementary material.

References

1. a Wang S, Huang P, Nie L, Xing R, Liu D, Wang Z, Lin J, Chen S, Niu G, Lu G, Chen X. *Adv. Mater.* 2013; 25:3055–3061. [PubMed: 23404693] b Huang P, Bao L, Zhang C, Lin J, Luo T, Yang D, He M, Li Z, Gao G, Gao B. *Biomaterials.* 2011; 32:9796–9809. [PubMed: 21917309] c Lovell JF, Jin CS, Huynh E, Jin H, Kim C, Rubinstein JL, Chan WCW, Cao W, Wang LV, Zheng G. *Nat. Mater.* 2011; 10:324–332. [PubMed: 21423187]
2. a Tian Q, Tang M, Sun Y, Zou R, Chen Z, Zhu M, Yang S, Wang J, Wang J, Hu J. *Adv. Mater.* 2011; 23:3542–3547. [PubMed: 21735487] b Zha Z, Yue X, Ren Q, Dai Z. *Adv. Mater.* 2012; 25:777–782. [PubMed: 23143782] c Tian Q, Jiang F, Zou R, Liu Q, Chen Z, Zhu M, Yang S, Wang J, Wang J, Hu J. *ACS Nano.* 2011; 5:9761–9771. [PubMed: 22059851] d Yang K, Zhang S, Zhang G, Sun X, Lee S-T, Liu Z. *Nano Lett.* 2010; 10:3318–3323. [PubMed: 20684528] e Yang K, Hu L, Ma X, Ye S, Cheng L, Shi X, Li C, Li Y, Liu Z. *Adv. Mater.* 2012; 24:1868–1872. [PubMed: 22378564] f Wang Y, Black KC, Luehmann H, Li W, Zhang Y, Cai X, Wan D, Liu S-Y, Li M, Kim P. *ACS Nano.* 2013; 7:2068–2077. [PubMed: 23383982] g Zhang Z, Wang J, Chen C. *Adv. Mater.* 2013; 25:3869–3880. [PubMed: 24048973] h Liu Y, Ai K, Liu J, Deng M, He Y, Lu L. *Adv. Mater.* 2012; 25:1353–1359. [PubMed: 23280690] i Cheng L, Yang K, Chen Q, Liu Z. *ACS Nano.* 2012; 6:5605–5613. [PubMed: 22616847] j Shan G, Weissleder R, Hilderbrand SA. *Theranostics.* 2013; 3:267–274. [PubMed: 23606913]
3. Yang K, Xu H, Cheng L, Sun C, Wang J, Liu Z. *Adv. Mater.* 2012; 24:5586–5592. [PubMed: 22907876]
4. a Cheng L, Yang K, Li Y, Chen J, Wang C, Shao M, Lee S-T, Liu Z. *Angew. Chem.* 2011; 123:7523–7528. b Zha Z, Deng Z, Li Y, Li C, Wang J, Wang S, Qu E, Dai Z. *Nanoscale.* 2013; 5:4462–4467. [PubMed: 23584573] c Tian Q, Hu J, Zhu Y, Zou R, Chen Z, Yang S, Li R-W, Su Q, Han Y, Liu X. *J Am. Chem. Soc.* 2013; 135:8571–8577. [PubMed: 23687972] d Xiong R, Soenen SJ, Braeckmans K, Skirtach AG. *Theranostics.* 2013; 3:141–151. [PubMed: 23471141]
5. a Lal S, Clare SE, Halas NJ. *Acc. Chem. Res.* 2008; 41:1842–1851. [PubMed: 19053240] b Huang X, Jain PK, El-Sayed IH, El-Sayed MA. *Nanomedicine.* 2007; 2:681–693. [PubMed: 17976030] c Li Z, Huang P, Zhang X, Lin J, Yang S, Liu B, Gao F, Xi P, Ren Q, Cui D. *Mol. Pharm.* 2009; 7:94–104. [PubMed: 19891496] d Huang P, Pandoli O, Wang X, Wang Z, Li Z, Zhang C, Chen F, Lin J, Cui D, Chen X. *Nano Res.* 2012; 5:630–639. e Zhang Z, Wang J, Chen C. *Theranostics.* 2013; 3:223–238. [PubMed: 23471510] f Lukianova-Hleb EY, Ren X, Townley D, Wu X, Kupferman ME, Lapotko DO. *Theranostics.* 2012; 2:976–987. [PubMed: 23139725]
6. Gad SC, Sharp KL, Montgomery C, Payne JD, Goodrich GP. *Int. J. Toxicol.* 2012; 31:584–594. [PubMed: 23212452]

7. Khlebtsov N, Bogatyrev V, Dykman L, Khlebtsov B, Staroverov S, Shirokov A, Matora L, Khanadeev V, Pylaev T, Tsyganova N. *Theranostics*. 2013; 3:167–180. [PubMed: 23471188]
8. a Lin J, Wang S, Huang P, Wang Z, Chen S, Niu G, Li W, He J, Cui D, Lu G. *ACS nano*. 2013; 7:5320–5329. [PubMed: 23721576] b He J, Huang X, Li Y-C, Liu Y, Babu T, Aronova MA, Wang S, Lu Z, Chen X, Nie Z. *J. Am. Chem. Soc.* 2013; 135:7974–7984. [PubMed: 23642094]
9. He J, Liu Y, Babu T, Wei Z, Nie Z. *J. Am. Chem. Soc.* 2012; 134:11342–11345. [PubMed: 22746265]
10. Gao B, Rozin M, Tao AR. *Nanoscale*. 2013; 5:5677–5691. [PubMed: 23703218]
11. Hessel CM, Pattani VP, Rasch M, Panthani MG, Koo B, Tunnell JW, Korgel BA. *Nano Lett.* 2011; 11:2560–2566. [PubMed: 21553924]
12. Gassner F, Owen A. *Polymer*. 1994; 35:2233–2236.
13. Huang P, Xu C, Lin J, Wang C, Wang X, Zhang C, Zhou X, Guo S, Cui D. *Theranostics*. 2011; 1:240–250. [PubMed: 21562631]
14. a Albanese A, Tang PS, Chan WCW. *Annu. Rev. Biomed. Eng.* 2012; 14:1–16. [PubMed: 22524388] b De Jonga WH, Hagensb WI, Krystekc P, Burgera MC, Sipsb AJAM, Geertsma RE. *Biomaterials*. 2008; 29:1912–1919. [PubMed: 18242692] c Moghimi SM, Hunter AC, Murray JC. *FASEB J.* 2005; 19:311–330. [PubMed: 15746175]
15. Huang X, Peng X, Wang Y, Wang Y, Shin DM, El-Sayed MA, Nie S. *ACS Nano*. 2010; 4:5887–5896. [PubMed: 20863096]



Scheme 1.

Self-assembly of biodegradable gold vesicles (BGVs) composed of poly(ethylene glycol)-*b*-poly(ϵ -caprolactone) (PEG-*b*-PCL) tethered GNPs *via* dot-line-plane-vesicle mode during the dialysis process. BGVs with ultra-strong plasmonic coupling effect are superior photoacoustic (PA) imaging and photothermal therapy (PTT) agents with improved clearance after the dissociation of assemblies. PA signal and PTT efficiency of BGVs are increased with the decrease of *d* (distance between adjacent GNPs).

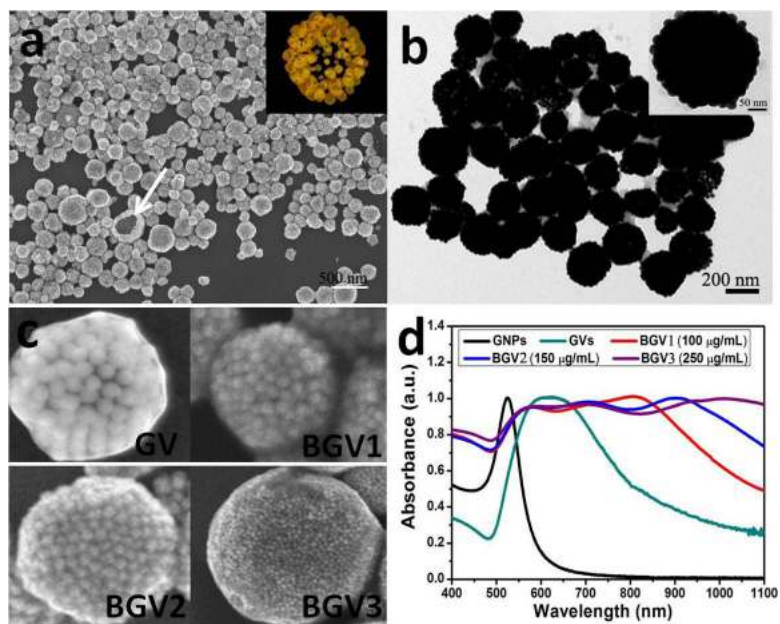


Figure 1.

Plasmonic BGVs self-assembled from GNPs (26.2 ± 1.45 nm). (a) SEM (Inset: 3-D electron density mapping of a broken BGV) and (b) TEM images (Inset: individual BGV). (c) SEM images of GV, BGV1, BGV2, and BGV3. (d) UV-vis-NIR spectra of GNPs, PEG-*b*-PS tethered gold vesicles (GVs), and block co-polymer (BCP)-tethered biodegradable gold vesicles produced by dialysis of 100, 150, and 250 100 μg/mL THF solution of GNPs. The LSPR peaks of BGVs can be tuned by varying the GNP concentration.

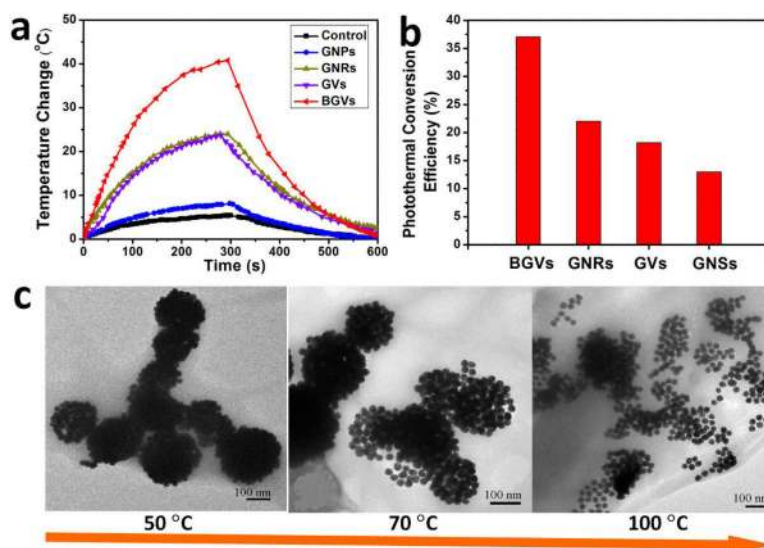
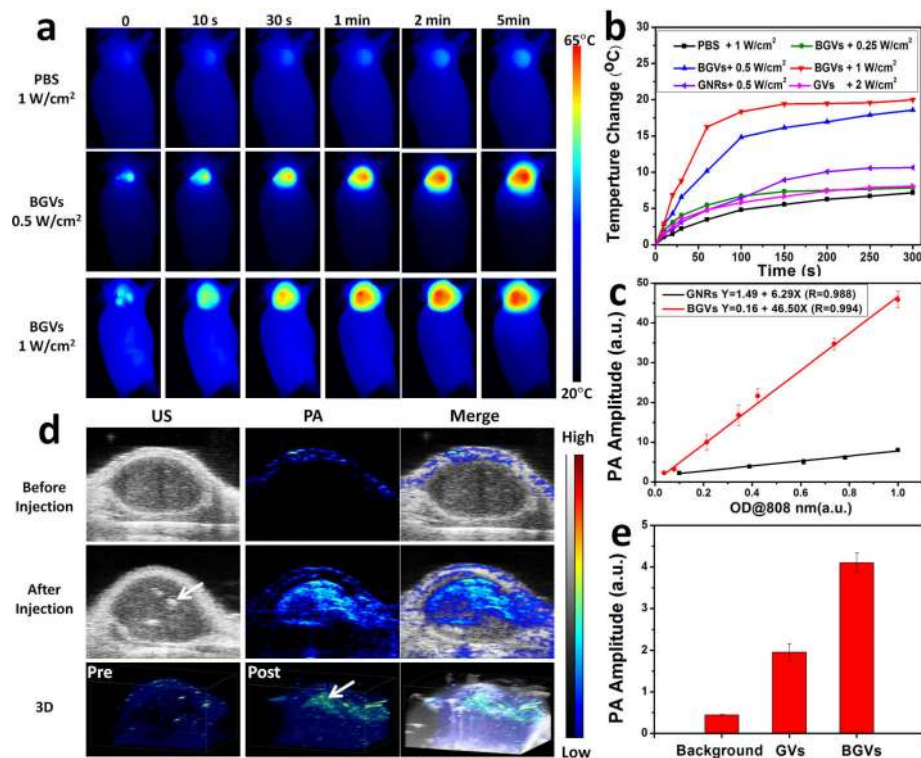


Figure 2.

(a) Temperature elevation of the aqueous solutions of GNPs, GNRs, GVs and BGVs exposed to laser (1 W/cm^2) as a function of irradiation time. GNPs (same Au concentration with BGVs, $\lambda_{\text{ex}} = 808 \text{ nm}$). GNRs ($\text{OD}@808 \text{ nm}=1$, $\lambda_{\text{ex}} = 808 \text{ nm}$). GVs ($\text{OD}@671 \text{ nm}=1$, $\lambda_{\text{ex}} = 671 \text{ nm}$). BGVs ($\text{OD}@808 \text{ nm}=1$, $\lambda_{\text{ex}} = 808 \text{ nm}$). The irradiation lasted for 5 min, and then the laser was turned off. Pure water was used as a negative control. (b) Photothermal conversion efficiencies of BGVs, GVs, GNRs and GNSs. (c) TEM images of BGVs after being treated at different temperatures for 10 min.

**Figure 3.**

(a) Thermal images of MDA-MB-435 tumor-bearing mice exposed to 808 nm laser for 5 min at post-injection of PBS or BGVs. (b) Heating curves of tumors upon laser irradiation as a function of irradiation time. (c) PA signals of BGVs and GNRs as a function of optical density. (d) *In vivo* 2D and 3D ultrasonic (US) and photoacoustic (PA) images of tumor tissues at pre-injection and post-injection of BGVs. Arrows indicate the location of BGVs. (e) PA intensities of tumor tissues with intratumoral administration of the same amount of GVs or BGVs.

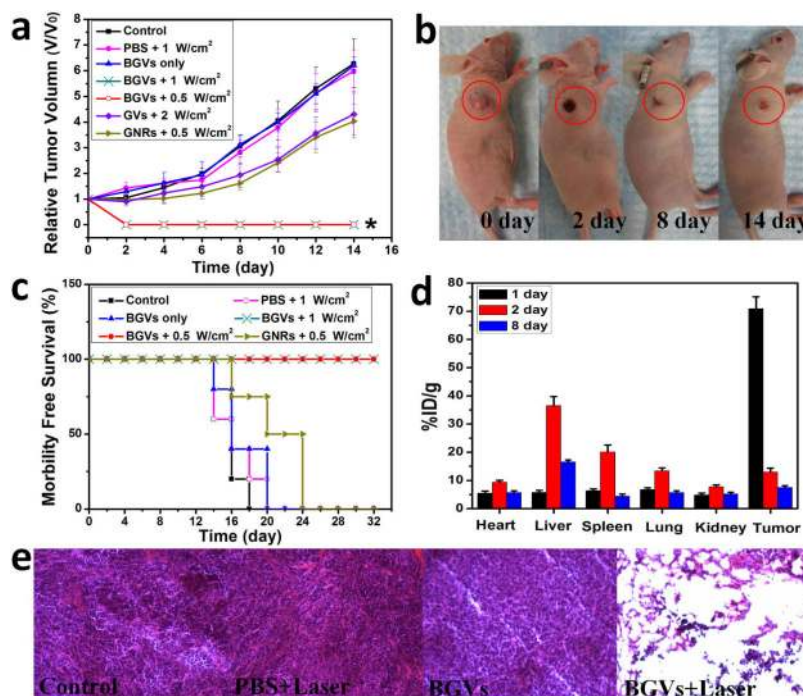


Figure 4.

(a) Tumor growth curves of different groups of MDA-MB-435 tumor-bearing mice after treatment. Tumor volumes were normalized to their initial sizes. Error bars represent the standard deviations of 5-7 mice per group. Asterisk indicates $P < 0.01$. (b) The photographs of MDA-MB-435 tumor-bearing mice at different days after BGV treatment. (c) Survival curves of tumor-bearing mice after various treatments. BGVs injected mice after PTT treatment showed 100% survival over 30 days. (d) Pharmacokinetics of BGVs after intratumoral injection of 50 μ L of BGVs (400 μ g/mL). Inductively coupled plasma mass spectrometry (ICP-MS) analysis of Au in different organs at 1, 2 and 8 days post-injection ($n = 3$ /group). (e) H&E staining of tumor sections collected from different groups of mice after laser irradiation.